Supporting Information

Structure-Designed Synthesis of 3D MoS_2 Anchored into Ionic Liquid Modified rGO-CNTs Inspired by Honeycomb for Excellent Lithium Storage

Jun Xia,[a] Ruixing Li,[a] Tianshuai Wang,[a] Puheng Yang,[b] Heliang Zhou,[a] Jiajie Li, [b] Gangyi Xiong,[a] Yalan Xing [,a] and Shichao Zhang [*,a]*

a. School of Materials Science and Engineering, Beihang University, Beijing 100191, P.R. China.
b. School of Physics Science and Nuclear Energy Engineering, Beihang University, Beijing 100191, P.R. China.

**E-mail:* csc@buaa.edu.cn*;* xingyalan@buaa.edu.cn.

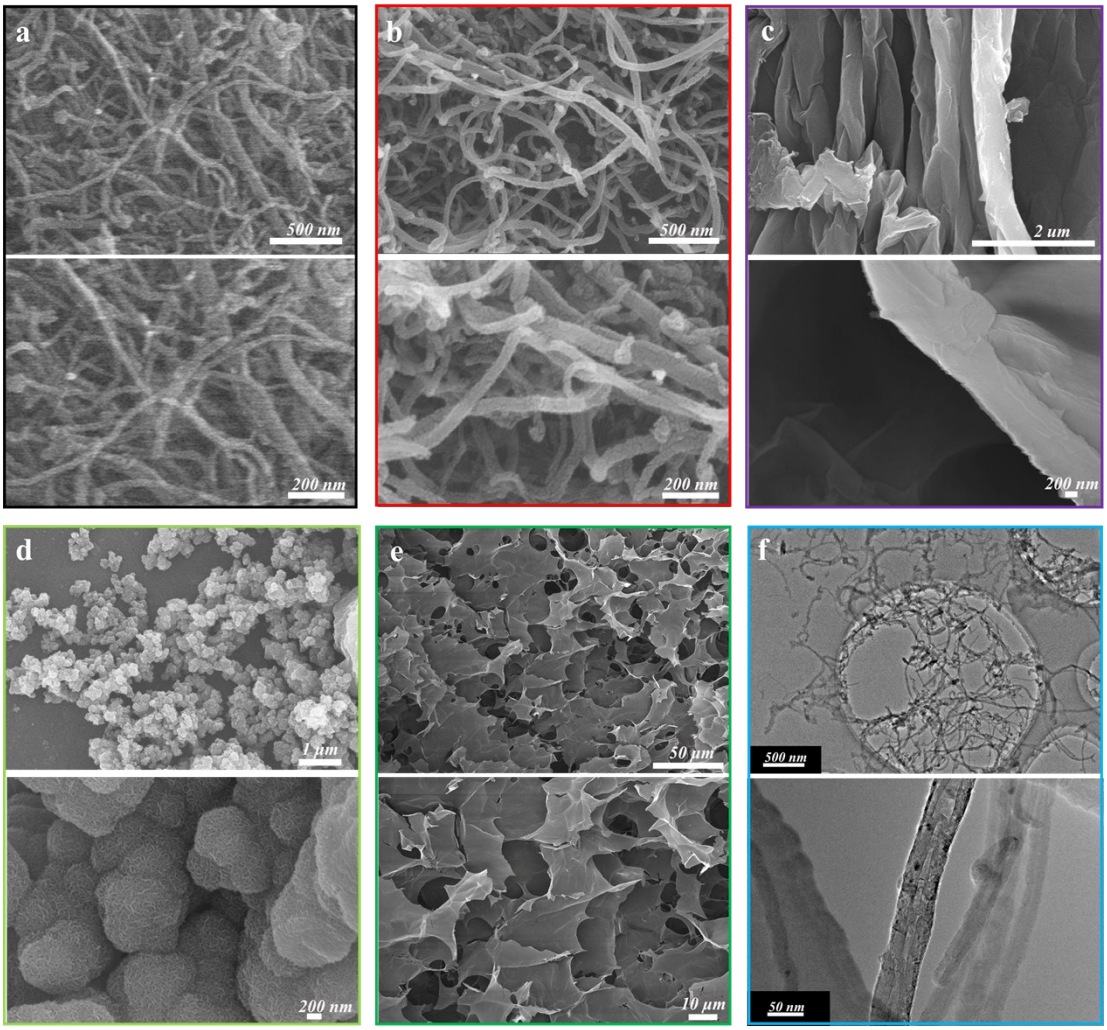

Figure S1. a) FE-SEM images of CNTs before treatment and b) surface functionalized CNTs, c) GO sheets, d) MoS_2 grown in solution without GO−CNTs−IL substrate, e) GO−CNTs−IL aerogel. f) TEM images of surface functionalized CNTs.

Firstly, we fabricated surface functionalized CNTs with extremely hydrophilic property from multiwalled CNTs. Subsequently, hydrophilic CNTs were dispersed to the aqueous colloidal suspension of GO sheets to obtain GO−CNTs−IL aerogel.

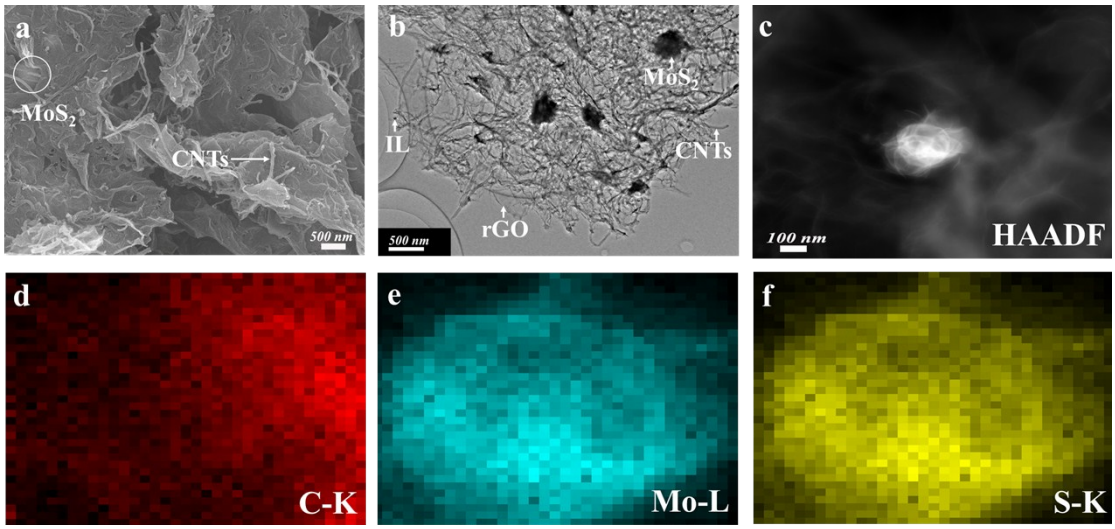

Figure S2. a) FE-SEM, b) TEM images of MoS_2@rGO−CNTs−IL. c-f) HAADF-STEM image of MoS_2@rGO−CNTs−IL and EDS mappings of C (red), Mo (blue) and S (yellow) in low magnification.

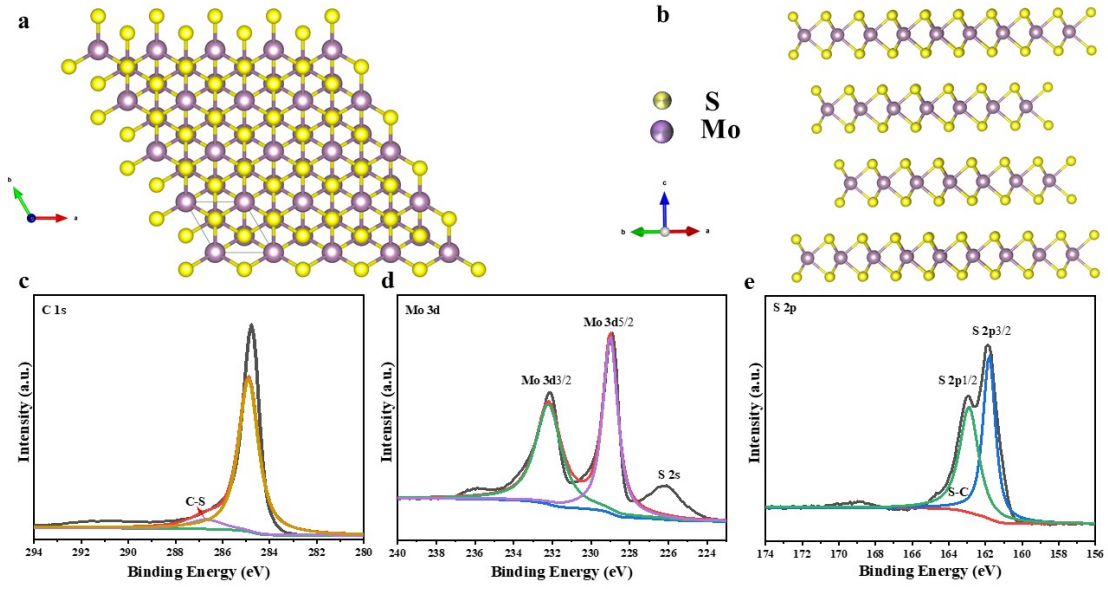

Figure S3. a, b) The crystal structures of MoS_2 with (001) and (110) crystal planes. c-e) XPS spectra of C 1s, Mo 3d, and S 2p, respectively.

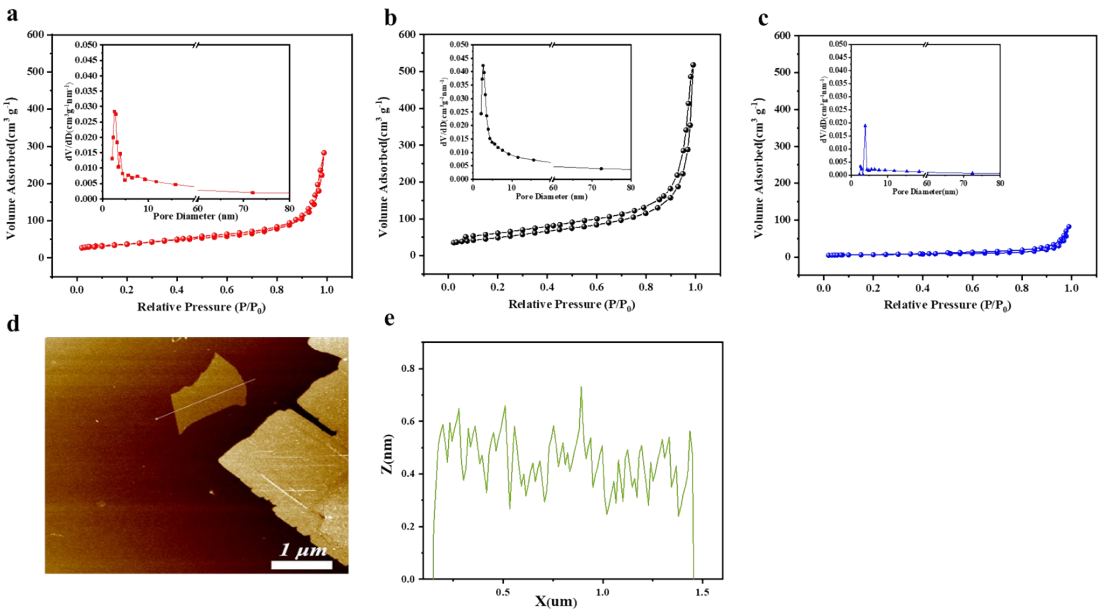

Figure S4. a-c) N_2 adsorption/desorption isotherms of MoS_2@rGO−CNTs−IL, rGO−CNTs−IL and pure MoS_2 (The insets show BJH pore size distribution plots curves). d, e) Representative AFM image of individual GO nanosheets and AFM image corresponding linear scan analysis of the GO nanosheets.

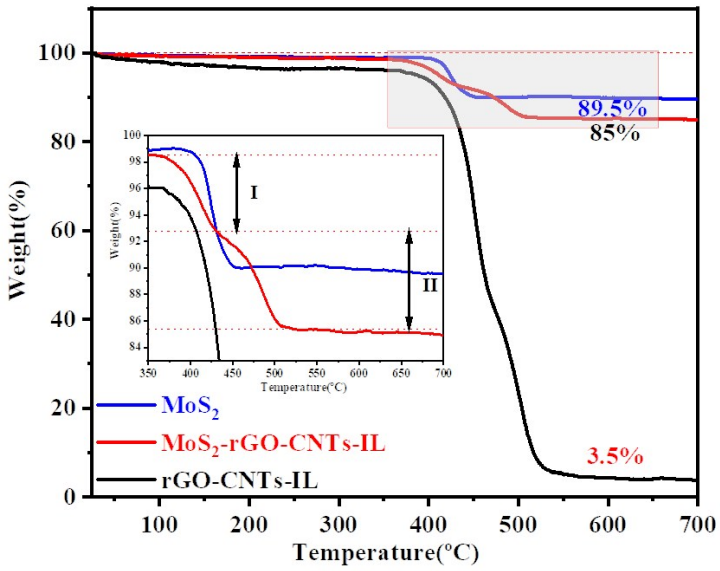

Figure S5. Thermogravimetric analysis (TGA) of MoS_2@rGO−CNTs−IL, rGO−CNTs−IL and pure MoS_2 sample (The inset shows the enlarged image).

Table S1. Nyquist plots with MoS_2@rGO−CNTs−IL electrodes before 1st, after 200th and 500th cycles.

Electrode	R_s	R_{SEI}	R_{ct}	Cycles
MoS_2@rGO−CNTs−IL	2.4	8.3	119.7	Before 1st
	4.2	7.9	20.4	After 200th
	5.5	6.1	51.8	After 500th

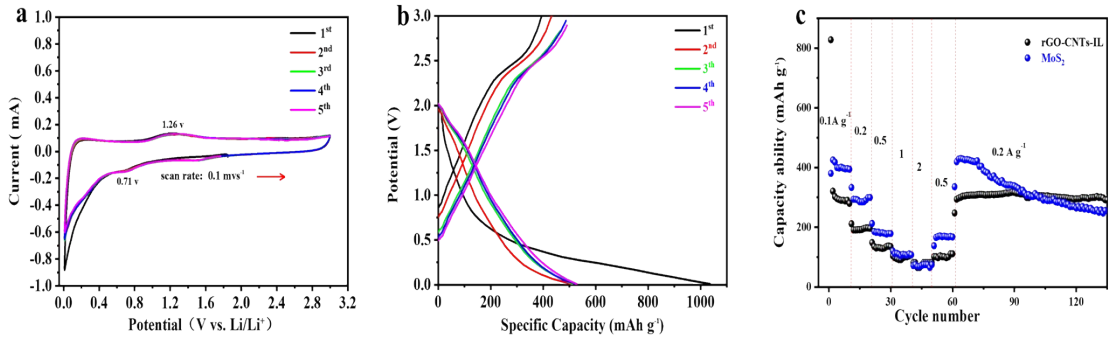

Figure S6. a) CV curves of rGO−CNTs−IL at a scanning rate of 0.1 mV s^{-1}. b) Charge-discharge curves of rGO−CNTs−IL for the first five cycles at a current density of 100 mA g^{-1}. c) Rate performance of rGO−CNTs−IL and MoS_2 electrodes with various current densities from 0.1 to 2 A g^{-1}.

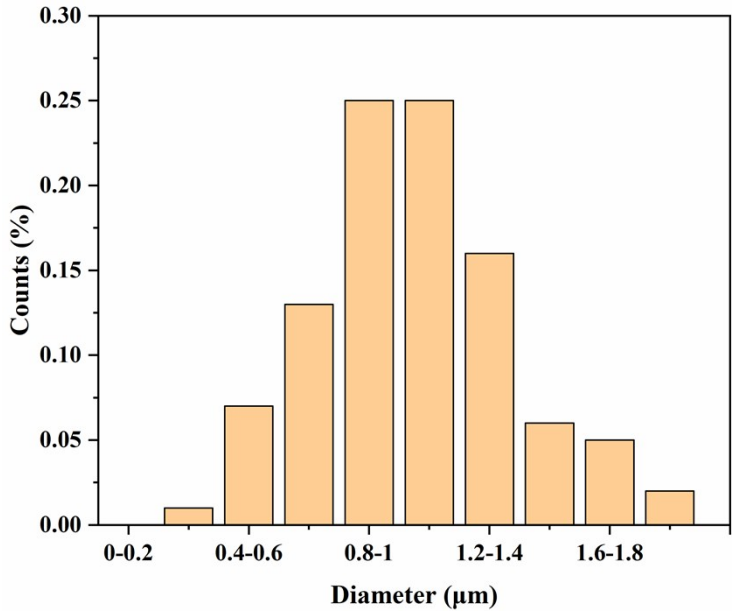

Figure S7. The particle size distribution of MoS_2@rGO−CNTs−IL.

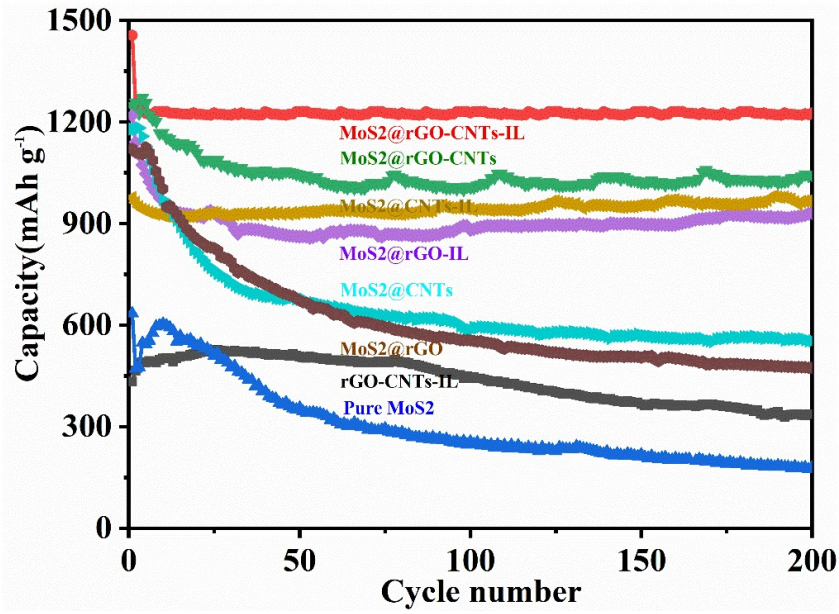

Figure S8. Cycling capacitance of MoS_2@rGO−CNTs−IL, MoS_2@rGO−CNTs, MoS_2@ CNTs−IL, MoS_2@rGO−IL, MoS_2@CNTs, MoS_2@rGO, rGO−CNTs−IL and MoS_2 electrodes at a current density of 200 mA g^{-1}.

In order to better explain the function of each carbon component of MoS_2@rGO−CNTs−IL, we constructed MoS_2-based electrodes with different carbon component separately. Eight samples were prepared and marked as pure MoS_2, rGO-

CNTs-IL, MoS_2@rGO, MoS_2@CNTs, MoS_2@rGO-IL, MoS_2@CNTs-IL, MoS_2@rGO-CNTs and MoS_2@rGO-CNTs-IL. The cycling performance of all eight electrodes at a current density of 200 mA g^{-1} are presented in Figure S8, MoS_2@rGO−CNTs−IL electrode shows the best performance. It can be found that the cell with MoS_2 electrode shows a low capacity of 635 mAh g^{-1} in the first cycle and only remains 178 mAh g^{-1} after 200 cycles (in Figure S8), due to the low conductivity and serious volume effects simultaneously. The electrochemical property of MoS_2 increases first and then decays quickly. For rGO−CNTs−IL electrode, it shows the lowest initial capacity among the eight cells and then the capacity decays gradually.

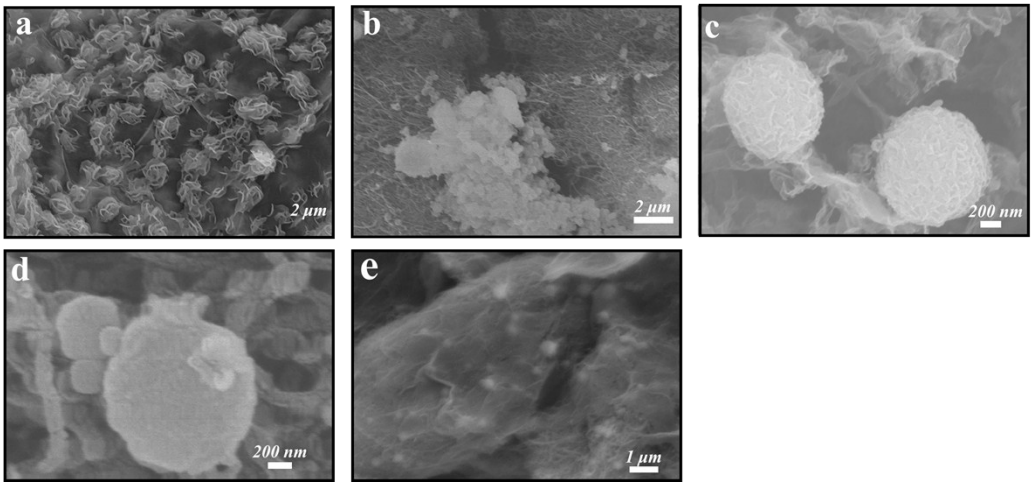

Figure S9. FE-SEM images of a) MoS_2@rGO, b) MoS_2@CNTs, c) MoS_2@rGO−IL, d) MoS_2@CNTs−IL and e) MoS_2@rGO−CNTs.

As shown in Figure S8, the MoS_2@rGO electrode exhibits a high capacity of 1120 mAh g^{-1} because of the assistance of rGO. However, we can find that both graphene and MoS_2 are severely agglomerated in Figure S9a. Therefore, the capacity of MoS_2@rGO decays significantly after several cycles and only remains 474 mAh g^{-1} after 200 cycles. The electrochemical property of MoS_2@CNTs are displayed in Figure S8. The cyclic property also decays significantly with cycles. The initial discharge capacity of MoS_2@CNTs is almost 1180 mAh g^{-1}. Similarly, we can observe that both CNTs and MoS_2 are severely agglomerated in Figure S9b. Hence, the capacity of MoS_2@CNTs decays significantly after 40 cycles and remains 550 mAh g^{-1} after 200

cycles. The improvement of MoS_2@rGO and MoS_2@CNTs indicates the existence of rGO and CNTs could enhance the electrical conductivity of pure MoS_2 and lead to higher initial capacity. But the unsatisfactory cyclic performance and their SEM images imply the dispersion of MoS_2 is not even and volume expansion induced pulverization is not addressed by such structure.

When IL is introduced, the MoS_2@rGO−IL and MoS_2@CNTs-IL electrode show improved long-term cyclic performance (Figure S9c and Figure S9d). For MoS_2@rGO−IL, its reversible capacity gradually declined from an initial capacity of 1104 to 940 mAh g^{-1} after 20 cycles, giving rise to a 85% capacity retention. After 20 cycles, it maintains ~900 mAh g^{-1} until the end of 200 cycles. MoS_2@CNTs-IL exhibits similar feature and delivers a capacity of ~940 mAh g^{-1} from the 20th cycle to the 200th cycle. The improvement indicates IL is very helpful in constructing the hybrid electrode. Figure S9c and Figure S9d display the SEM images of MoS_2@rGO−IL and MoS_2@CNTs-IL, rGO/CNTs and MoS_2 are more evenly distributed with the assistance of IL. This proves ionic liquid could facilitate the incorporation and dispersion of MoS_2 on rGO/CNTs matrix. Moreover, IL can improve the stability of the electrode and increase the binding force of graphene and MoS_2. In addition, the small amount of ionic liquid would be carbonized after calcination and turn into carbon coating to improve the electrochemical performance of MoS_2.

In Figure S8, we can also find that the MoS_2@rGO−CNTs electrode decays in the initial 50 cycles, and then it keeps stable in the following cycles. The MoS_2@rGO−CNTs delivers a reversible specific capacity about 1248 mAh g^{-1} in the first several cycles and remains almost ~1000 mAh g^{-1} after 200 cycles. SEM images shown in Figure S9e indicate MoS_2 is unevenly distributed on rGO-CNT matrix without the assistance of IL. It should be noted that graphene and functional CNTs have been considered as highly conductive matrix. rGO-CNT matrix possesses multimodal porous structure, including the micro-mesopores, meso- and macropores. It has been widely recognized that the creation of the interpenetrating and hierarchical pores are effective ways to guarantee the sufficient contact area and plenty of electrochemical active sites between electrolyte and electrode materials.

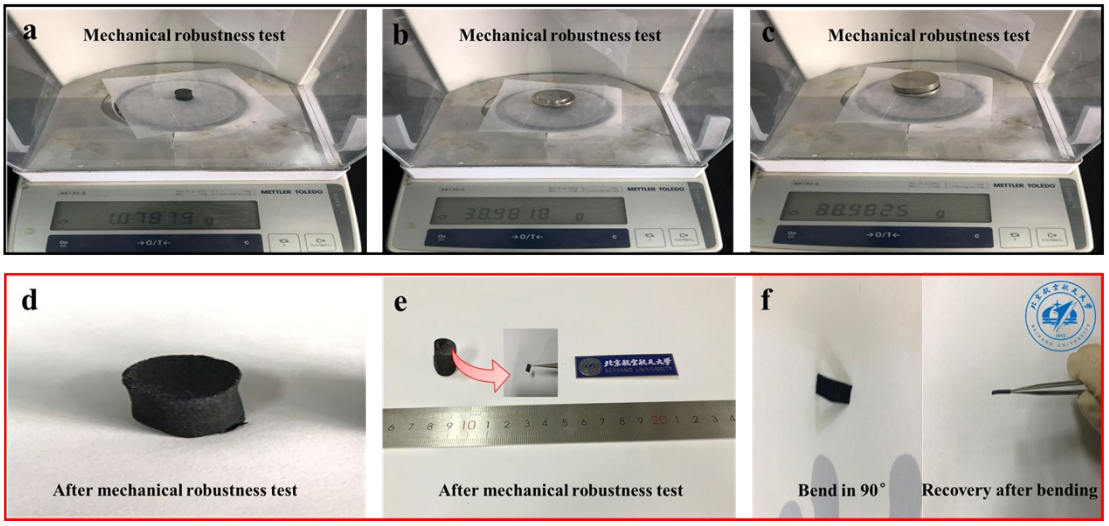

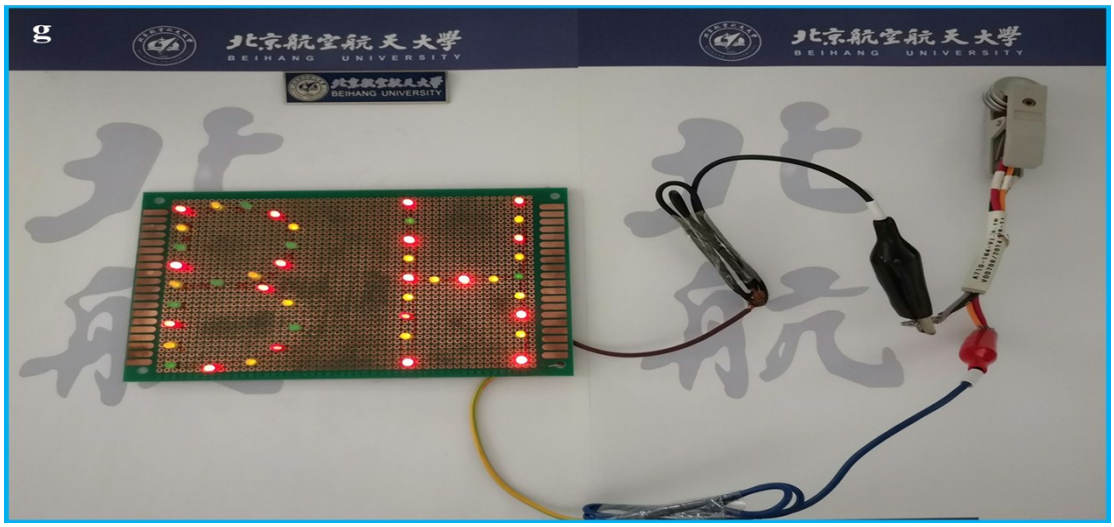

Figure S10. Photographs of the mechanical robustness (a-c) and flexible tests (d-f) for MoS2@rGO−CNTs−IL aerogel. g) Photo of the LED beads lighted by the MoS2@rGO−CNTs−IL cells.

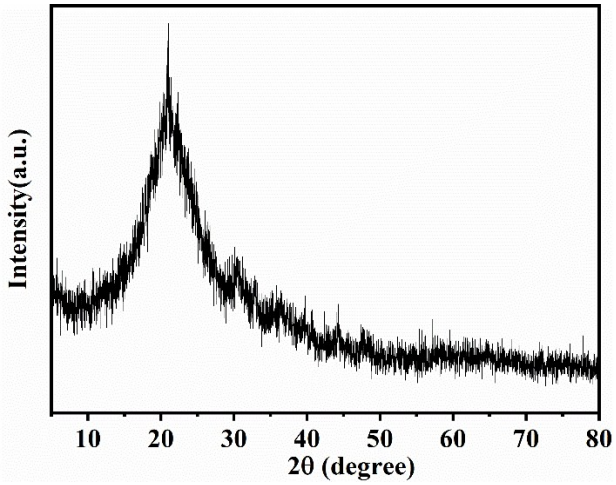

Figure S11. XRD of MoS_2@rGO−CNTs−IL after 1000 cycles at 5 A g^{-1}.

Table S2. Comparison of the reported MoS_2-based electrode materials for lithium ion storage.

Electrode	**1st Specific capacity (m Ah g^{-1})**	**1st Coulombic efficiency (%)**	**Capacity decay rate (%) [at (x) A g^{-1} after (y) cycles]**	**Rate performance**
3D highly porous SHS MoS_2@rGO−CNTs−IL (**this work**)	1456 at 200 mA g^{-1}	83.3	0.0075 (5,1000)	1206, 1143, 1079, 1005 and 712 $mAhg^{-1}$ at 0.2, 0.5, 1, 2 and 5 A g^{-1}
MoS_2 -Graphene-Carbon Nanotube [1]	929 at 1000 mA g^{-1}	74	0.046 (1, 100)	949, 883, 858, 737 and 652 $mAhg^{-1}$ at 0.1, 0.5, 1, 5 and 10 A g^{-1}
CNT@MoS_2@C [2]	1238 at 100 mA g^{-1}	76.3	0.006 (1, 500)	949, 883, 858, 737 and 652 $mAhg^{-1}$ at 0.1, 0.5, 1, 5 and 10 A g^{-1}
MoS_2-G [3]	1160 at 100 mA g^{-1}	77.2	0.036 (1, 500)	1035, 1012, 986 and 890 $mAhg^{-1}$ at 0.2, 0.3, 0.5 and 1 A g^{-1}
Honeycomb-like MoS_2 nanoarchitectures on 3DGF [4]	1397 at 200 mA g^{-1}	82.9	0.2 (0.2, 60)	1172, 1095, 1007, 966 and 800 $mAhg^{-1}$ at 0.2, 0.5, 1, 2 and 5 A g^{-1}
MoS_2/GA–GF free-standing hybrid [5]	1404 at 200 mA g^{-1}	81.7	0.065 (1, 500)	993, 894, 789, 689 and 593 $mAhg^{-1}$ at 0.2, 0.5, 1, 2 and 5 A g^{-1}
MoS_2 3D assembled tubes [6]	1172 at 100 mA g^{-1}	68.3	0.57 (0.1, 50)	900, 825, 600 and 500 $mAhg^{-1}$ at 0.1, 0.5, 1 and 5 A g^{-1}
hierarchical hollow MoS_2 nanoparticles [7]	1236 at 100 mA g^{-1}	74	0.34 (0.1, 80)	1030, 910, 850 and 780 $mAhg^{-1}$ at 0.1, 0.3, 0.5

				and 1 A g^{-1}
GF@CNT@MoS_2 [8]	1364 at 100 mA g^{-1}	68.3	0.17 (0.2, 200)	925, 541, 408, 316 and 229 $mAhg^{-1}$ at 0.1, 0.5, 1, 2 and 5 A g^{-1}
CNFs@MoS_2 [9]	1489 at 100 mA g^{-1}	66	0.05 (1, 300)	1000, 1100, 900 and 864 $mAhg^{-1}$ 0.1, 0.5, 1, 2 and 5 A g^{-1}
MoS_2/G [10]	1346 at 100 mA g^{-1}	69.1	0.02 (0.1, 50)	1040, 1000, 820 and 702 $mAhg^{-1}$ at 0.1, 0.2, 0.5 and 1 A g^{-1}
MoS_2-PPY-rGO [11]	1428 at 200 mA g^{-1}	75.9	0.007 (0.2, 400)	1100, 910, 800 and 600 $mAhg^{-1}$ 0.2, 0.5, 1 and 2 A g^{-1}
MoS_2-SWNT [12]	1117 at 200 mA g^{-1}	64.4	0.11 (0.1, 100)	915, 850, 720, 630 and 586 $mAhg^{-1}$ 0.1, 0.4, 1.2, 2.4 and 3.2 A g^{-1}
MW-MoS_2 [13]	1199 at 500 mA g^{-1}	75	0.037 (5, 490)	1355, 1100, 980, 720 and 438 $mAhg^{-1}$ 0.5, 1, 2, 5 and 10 A g^{-1}
MoS_2−0.5nm-TiO_2 [14]	1393 at 100 mA g^{-1}	69	0.4 (0.5, 200)	850, 600, 500 and 392 $mAhg^{-1}$ 0.05, 0.2, 0.4 and 0.8 A g^{-1}
NTL-MoS_2 /G hybrid [15]	1665 at 100 mA g^{-1}	67.7	0.19 (0.1, 200)	1100, 1050, 950 and 650 $mAhg^{-1}$ 0.1, 0.2, 0.5 and 1 A g^{-1}
GR/CNT-MoS_2 (3) hybrid [16]	1522 at 100 mA g^{-1}	82.1	0.04 (1, 600)	1150, 1000, 950 and 900 $mAhg^{-1}$ 0.1, 0.2, 0.5 and 1 A g^{-1}

References:

[1] Zhu, C.; Mu, X.; Aken, P. A.; Maier, J.; Yu, Y., Fast Li Storage in MoS_2-Graphene-Carbon Nanotube Nanocomposites: Advantageous Functional Integration of 0D, 1D, and 2D Nanostructures. *Adv. Energy Mater.* **2015**, 5, 1401170.

[2] Zhang, Z.; Zhao, H.; Teng, Y.; Chang, X.; Xia, Q.; Li, Z.; Fang, J.; Du, Z.; Świerczek, K. Carbon-Sheathed MoS_2 Nanothorns Epitaxially Grown on CNTs: Electrochemical Application for Highly Stable and Ultrafast Lithium Storage. *Adv. Energy Mater.* **2018**, 8, 1700174.

[3] Teng, Y.; Zhao, H.; Zhang, Z.; Li, Z.; Xia, Q.; Zhang, Y.; Zhao, L.; Du, X.; Du, Z.; Lv, P.; Świerczek, K. MoS_2 Nanosheets Vertically Grown on Graphene Sheets for Lithium-Ion Battery Anodes. *ACS Nano* **2014**, 8, 5164.

[4] Wang, J.; Liu, J.; Chao, D.; Yan, J.; Lin, J.; Shen, Z. X. Self-assembly of honeycomb-like MoS_2 nanoarchitectures anchored into graphene foam for enhanced lithium-ion storage. *Adv. Mater.* **2014**, 26, 7162.

[5] Wang, W.; Yang, P.; Jian, Z.; Li, H.; Xing, Y.; Zhang, S. Rational design of a 3D MoS_2/dual-channel graphene framework hybrid as a free-standing electrode for enhanced lithium storage. *J. Mater. Chem. A* **2018**, 6, 13797.

[6] Wang, P. P.; Sun, H.; Ji, Y.; Li, W.; Wang, X. Three-dimensional assembly of single-layered MoS_2. *Adv. Mater.* **2014**, 26, 964.

[7] Wang, M.; Li, G.; Xu, H.; Qian, Y.; Yang, J. Enhanced lithium storage performances of hierarchical hollow MoS_2 nanoparticles assembled from nanosheets. *ACS Appl. Mater. Interfaces* **2013**, 5, 1003.

[8] Ren, J.; Ren, R. P.; Lv, Y. K. A flexible 3D graphene@CNT@MoS_2 hybrid foam anode for high-performance lithium-ion battery. *Chemical Engineering Journal* **2018**, 353, 419.

[9] Zhou, F.; Xin, S.; Liang, H. W.; Song, L. T.; Yu, S. H. Carbon nanofibers decorated with molybdenum disulfide nanosheets: synergistic lithium storage and enhanced electrochemical performance. *Angew. Chem. Int. Ed*. **2014**, 53, 11552.

[10] Ye, J.; Chen, W.; Chen, Q.; Yu, Z.; Lee, J. Y. Poly-assisted synthesis of MoS_2

/graphene composites with enhanced electrochemical performances for reversible lithium storage. *Electrochim. Acta* **2016**, 190, 538.

[11] Xie, D.; Wang, D. H.; Tang, W. J.; Xia, X. H.; Zhang, Y. J.; Wang, X. L.; Gu, C. D.; Tu, J. P. Binder-free network-enabled MoS_2-PPY-rGO ternary electrode for high capacity and excellent stability of lithium storage. *J. Power Sources* **2016**, 307, 510.

[12] Wang, J. Z.; Lu, L.; Lotya, M.; Coleman, J. N.; Chou, S. L.; Liu, H. K.; Minett, A. I.; Chen, J. Development of MoS_2-CNT Composite Thin Film from Layered MoS_2 for Lithium Batteries. *Adv. Energy Mater.* **2013**, 3, 789.

[13] Tian, X.; Gao, Q.; Zhang, H.; Li, Z.; Xiao, H.; Zhang, Q.; Ma, L. Uniform small-sized MoS_2 from novel solution-based microwave-assisted method with exceptional reversible lithium storage properties. *Nanoscale* **2018**, 10, 15222.

[14] Ren, W.; Zhou, W.; Zhang, H.; Cheng, C. ALD TiO_2-Coated Flower-like MoS_2 Nanosheets on Carbon Cloth as Sodium Ion Battery Anode with Enhanced Cycling Stability and Rate Capability. *ACS Appl. Mater. Interfaces* **2017**, 9, 487.

[15] Ma, L.; Ye, J.; Chen, W.; Chen, D.; Yang Lee, J. Gemini surfactant assisted hydrothermal synthesis of nanotile-like MoS_2/graphene hybrid with enhanced lithium storage performance. *Nano Energy* **2014**, 10, 144.

[16] Liu, M.; Liu, Y.; Tang, B.; Zhang, P.; Yan, Y.; Liu, T. 3D Conductive Network Supported Monolithic Molybdenum Disulfide Nanosheets for High-Performance Lithium Storage Applications. *Adv. Mater. Interfaces* **2017**, 4, 1601228.